



Article

Influences of Cu Doping on the Microstructure, Optical and Resistance Switching Properties of Zinc Oxide Thin Films

Jun-Hong Weng¹, Ming-Cheng Kao^{2,*} , Kai-Huang Chen³ and Men-Zhe Li⁴¹ Department of Electrical Engineering, Tunghai University, Taichung 40704, Taiwan; jhw@thu.edu.tw² Department of Information and Communication Engineering, Chaoyang University of Technology, Taichung 413310, Taiwan³ Department of Electronic Engineering, Center for Environmental Toxin and Emerging-Contaminant Research, Super Micro Mass Research & Technology Center, Cheng Shiu University, Chengcing Rd., Niasong District, Kaohsiung 83347, Taiwan; 5977@gcloud.csu.edu.tw⁴ Department of Electronic Engineering, Hsiuping University of Science and Technology, Taichung 41280, Taiwan

* Correspondence: kmc@cyut.edu.tw

Abstract: Copper-doped zinc oxide films ($Zn_{1-x}Cu_xO$) ($x = 0, 2\%, 4\%, 6\%$) were fabricated on conductive substrates using the sol-gel process. The crystal structure, optical and resistive switching properties of $Zn_{1-x}Cu_xO$ films are studied and discussed. RRAM is made using $Zn_{1-x}Cu_xO$ as the resistive layer. The results show that the (002) peak intensity and grain size of $Zn_{1-x}Cu_xO$ films increase from 0 to 6%. In addition, PL spectroscopy shows that the oxygen vacancy defect density of $Zn_{1-x}Cu_xO$ films also increases with the increase in Cu. The improved resistive switching performance of the RRAM device can be attributed to the formation of conductive filaments and the destruction of more oxygen vacancies in the $Zn_{1-x}Cu_xO$ film. Consequently, the RRAM device exhibits a higher low resistance state to high resistance state ratio and an HRS state of higher resistance value.

Keywords: ZnO; sol-gel; thin films; resistive switching

Citation: Weng, J.-H.; Kao, M.-C.; Chen, K.-H.; Li, M.-Z. Influences of Cu Doping on the Microstructure, Optical and Resistance Switching Properties of Zinc Oxide Thin Films. *Nanomaterials* **2023**, *13*, 2685. <https://doi.org/10.3390/nano13192685>

Academic Editor: Rodrigo Martins

Received: 9 August 2023

Revised: 28 September 2023

Accepted: 28 September 2023

Published: 30 September 2023

Correction Statement: This article has been republished with a minor change. The change does not affect the scientific content of the article and further details are available within the backmatter of the website version of this article.



Copyright: © 2023 by the authors. Licensee MDPI, Basel, Switzerland. This article is an open access article distributed under the terms and conditions of the Creative Commons Attribution (CC BY) license (<https://creativecommons.org/licenses/by/4.0/>).

1. Introduction

In recent research, resistive random access memory (RRAM) devices have been developed using various binary oxide materials, making them highly attractive for next-generation memory applications due to their fast operation, simple structure, low power consumption, nondestructive readout, long data retention, ease of fabrication, and cost-effectiveness [1–5]. Among the different oxide materials, ZnO-based semiconductor thin films are widely employed in RRAM devices. The ZnO-based semiconductor was investigated for its potential applications in RRAM, due to its low carrier trapping degree, non-toxicity, and simple chemical composition [6–10]. Recent studies have indicated that doping zinc oxide with transition metals can effectively reduce its intrinsic carrier density [11,12]. Specifically, La doping has been found to decrease the oxygen vacancy density in ZnO thin films, leading to an improved ON/OFF ratio in RRAM devices [13]. Numerous studies have also demonstrated RRAM characteristics in various doped ZnO thin films [14–18]. Additionally, researchers have explored Cu-doped ZnO materials, the grain size of which can be controlled by the amount of copper doping [19,20]. Cu is considered a suitable dopant for ZnO due to its similar ionic radii to Zn and its ability to act as a deep receptor, binding with adjacent O vacancies in the ZnO lattice [21,22].

We investigate the effects of copper on the electrical, structural, and switched resistive properties of $Zn_{1-x}Cu_xO$ thin films. The $Zn_{1-x}Cu_xO$ was synthesized on FTO substrates through the sol-gel process, followed by rapid thermal treatment. The crystallization and microstructure of the samples were analyzed using an X-ray diffractometer and a

scanning electron microscope, respectively. RRAM devices employing $Zn_{1-x}Cu_xO$ thin films were thoroughly examined, and their bipolar switching characteristics were analyzed and discussed.

2. Experimental Section

In this research, we prepared thin films of $Zn_{1-x}Cu_xO$ ($x = 0\%$, 2% , 4% , 6%) using the sol-gel process. $Zn_{1-x}Cu_xO$ films were prepared using a sol-gel method, employing zinc acetate dihydrate $(CH_3COO)_2Zn \cdot 2H_2O$ and copper acetate monohydrate $(Cu(CH_3COO)_2 \cdot 2H_2O)$ as precursor materials. The precursors were dissolved in 2-Methoxyethanol solvent to maintain a constant metal ion concentration of 0.05 M. Ethanolamine was added to ensure solution stability. These solutions were stirred at $60^\circ C$ for three hours using a magnetic stirrer and then allowed to stand for 72 h to obtain transparent solutions. The sol-gel solution was deposited onto a substrate mounted on a spin coater using a two-step spin process. The deposition step began with spinning at 1000 rpm for 10 s and then at 3000 rpm for 30 s. Subsequently, the samples were annealed on a hot plate at $300^\circ C$ for 2 min to remove the solvent. The entire process was repeated ten times to achieve the desired film thickness. Finally, the film was annealed at $600^\circ C$ for 2 min in a rapid annealing system. The annealing rate was $100^\circ C/min$. The thickness of $Zn_{1-x}Cu_xO$ film was 500 nm with α -step surface profiler.

Crystallization of samples was analyzed using XRD. To study the optical properties of $Zn_{1-x}Cu_xO$, we conducted transmittance optical measurements using a UV spectrometer. The effect of the fluorine-doped tin oxide (FTO) substrate was also taken into account during the transmittance correction. This is due to the fact that FTO substrate can absorb light in the UV-visible range. The transmittance may be measured inaccurately. We used a blank FTO substrate (without $Zn_{1-x}Cu_xO$ sample) for reference measurements. To correct for substrate effects, the transmittance of the FTO substrate alone was subtracted from the transmittance of the sample and substrate combination. These corrected transmittance data represent the transmittance of the $Zn_{1-x}Cu_xO$ sample without FTO substrate contribution. For analyzing optical emissions, photoluminescence spectroscopy was employed, covering a wavelength range from 350 nm to 600 nm. In addition, we characterized the switching properties of current-voltage for the $Zn_{1-x}Cu_xO$ thin films in RRAM. RRAM with a $Ag/Zn_{1-x}Cu_xO/FTO$ structure was measured using a semiconductor parameter analyzer. Figure 1 shows a schematic diagram of an RRAM device with Ag electrodes. One hundred circular top silver electrodes (100 nm thickness and 0.05 cm diameter) were fabricated on top of the $Zn_{1-x}Cu_xO$ layer using thermal evaporation technique at 5×10^{-6} torr.

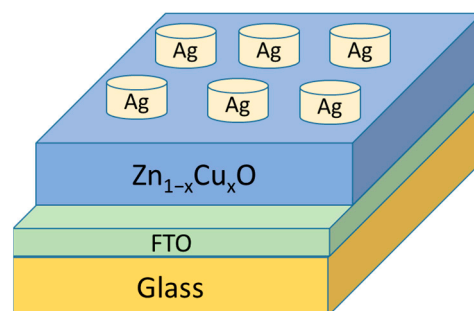


Figure 1. RRAM structure of $Ag/Zn_{1-x}Cu_xO/FTO$.

3. Results and Discussion

Figure 2 displays the XRD for $Zn_{1-x}Cu_xO$ with various Cu concentrations, compared with the pure zinc oxide. The XRD patterns match the standard JCPDS data (36-1451), indicating the absence of a rutile phase or any other phase. All samples have a wurtzite hexagonal structure oriented along the c -axis and a symmetric $P63/mc$ structure. There is no evidence of phase separation in the $Zn_{1-x}Cu_xO$ thin films with the replacement of Zn with Cu ions. In addition, there are no diffraction peaks of other impurities or compounds,

indicating that copper ions have been doped into the ZnO lattice to replace zinc ions. The (002) peak intensity of $Zn_{1-x}Cu_xO$ films increases with the Cu doping content from 2% to 6%. The samples exhibit a (002) peak of ZnO at approximately $2\theta = 34.5^\circ$. The enhanced (002) peak intensity with a higher Cu concentration can be attributed to lattice strain introduced by the size difference between Cu and Zn ions when Cu ions replace Zn ions in the ZnO lattice. The increased intensity of the (002) diffraction peak at approximately $2\theta = 34.5^\circ$ indicates a more ordered and periodic arrangement of atoms in the lattice along the c-axis. Lattice strain caused by the size mismatch between copper and zinc ions leads to this increase in order. When the atomic planes along the c-axis are more regularly spaced, the X-rays diffract more efficiently, resulting in higher intensity peaks in the XRD pattern. Strain affects the crystal structure and orientation of ZnO, resulting in greater distortion and increased (002) peak intensity as the Cu concentration rises.

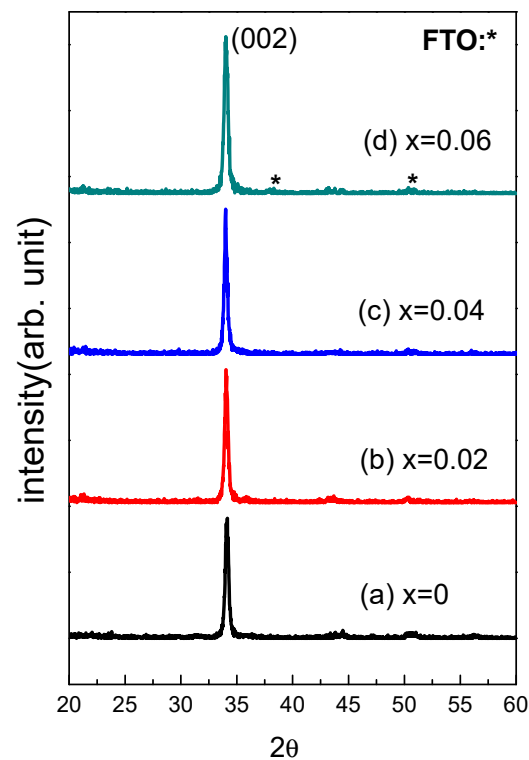


Figure 2. The patterns of XRD for $Zn_{1-x}Cu_xO$ films.

FWHM reflects the change in the average size of $Zn_{1-x}Cu_xO$ grains. The grain size of $Zn_{1-x}Cu_xO$ decreases with increasing FWHM. Specifically, a slight increase in FWHM was observed as the Cu concentration increased from 0% to 6%. Average sizes of grains for films, calculated using the Scherrer formula, were 20.3 nm for 0%, 15.2 nm for 2%, 9.5 nm for 4%, and 8.6 nm for 6%, respectively [23]. Figure 3 displays the surface morphology of the $Zn_{1-x}Cu_xO$ films, showing granular porous surfaces for all samples. It is evident that grain size decreases with the increase in the Cu concentration. This phenomenon can be attributed to the crystal structure and growth of the material. When copper is introduced into the zinc oxide lattice, copper (Cu) and zinc (Zn) have different atomic sizes and lattice constants, creating a lattice mismatch. The lattice mismatch in the $Zn_{1-x}Cu_xO$ film causes crystal strain in the crystal structure and hinders the growth of larger grains. In addition, the surface density of films increases as the Cu concentration rises. Furthermore, the thickness of all samples was found to be 500 nm.

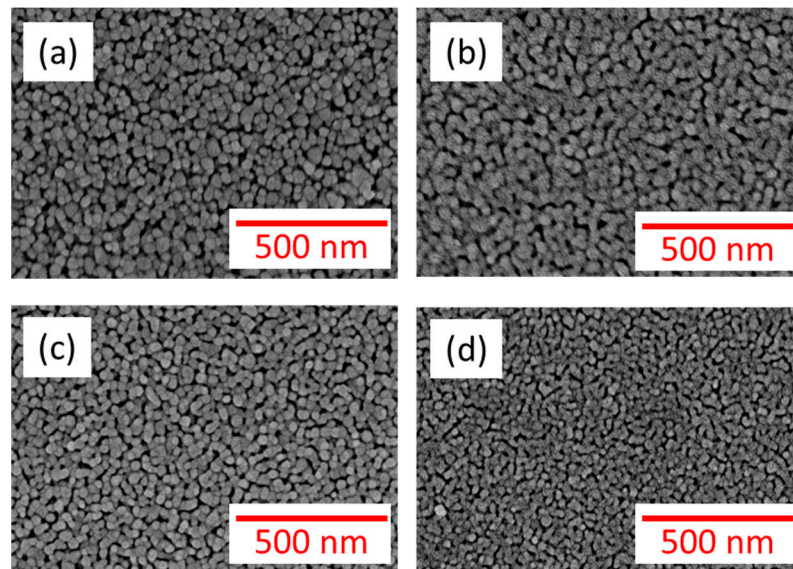


Figure 3. The images of SEM for $Zn_{1-x}Cu_xO$ films of (a) $x = 0$, (b) $x = 2\%$, (c) $x = 4\%$, and (d) $x = 6\%$.

Figure 4 shows the photoluminescence (PL) spectrum of $Zn_{1-x}Cu_xO$ at room temperature. The PL spectrum of ZnO exhibits two main components: one in the ultraviolet region and the other in the yellow-green visible region. The ultraviolet emission band at 385 nm shows the transition of electrons from the bottom of the conduction band to the zinc vacancy energy level [24,25]. Multiple yellow-green emissions observed in $Zn_{1-x}Cu_xO$ films are attributed to oxygen vacancy defects, which correspond to the transition from the conduction band to oxygen vacancy defects [26]. The ultraviolet emission at 385 nm of the $Zn_{1-x}Cu_xO$ thin film increases as the copper content increases. This may be due to the copper doping causing more zinc vacancy energy levels in the ZnO thin film, which enhances the ultraviolet emission. In addition, the yellow-green light emission of $Zn_{1-x}Cu_xO$ thin film increases with the increase in the copper doping amount. This enhancement may be caused by the replacement of copper ions into the ZnO lattice to form $Zn_{1-x}Cu_xO$, and more copper ions generate more oxygen vacancy defects in zinc oxide. Therefore, the transition from the conduction band to oxygen vacancy defects will also increase, resulting in an increase in yellow-green light emission in the $Zn_{1-x}Cu_xO$ thin film.

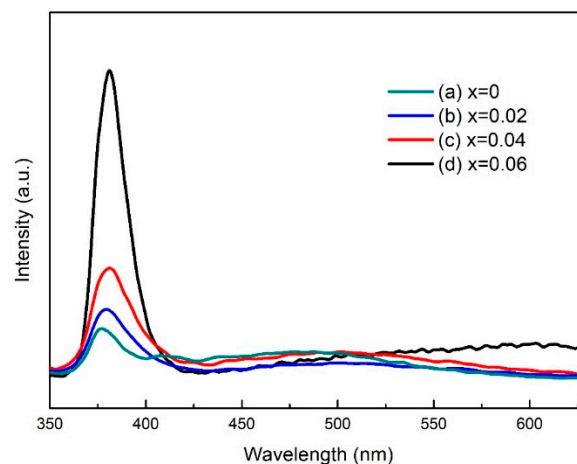


Figure 4. Photoluminescence (PL) spectra of $Zn_{1-x}Cu_xO$ films of (a) $x = 0$, (b) $x = 2\%$, (c) $x = 4\%$, and (d) $x = 6\%$.

Transmission spectra with a range of 300–800 nm for $Zn_{1-x}Cu_xO$ are shown in Figure 5. As the doping of Cu increases from 0% to 6%, the light transmittance for the $Zn_{1-x}Cu_xO$

film decreases from 92% to 78%. To determine the absorption coefficient and bandgap of these films, graphical methods were employed. The value of $(\alpha hv)^2$ can be obtained from the equation $\alpha hv = A(hv - E_g)^n$. In addition, the value of α can be obtained using the equation $\alpha = -(1/D)\ln T$ [27], where T is the transmittance, A is a function of the refractive index and hole/electron effective masses, h is the constant of Planck, v is the frequency of photons, and E_g is the bandgap. For a direct bandgap semiconductor ($n = 1/2$), the bandgaps of all films were calculated via the extrapolation of the straight portion for the curve of $(\alpha hv)^2 = 0$ in Figure 6. The inset of Figure 6 shows the relationship between the Cu doping amount and sample band gap energy. As the Cu content increases from 0 to 6%, the bandgap in $Zn_{1-x}Cu_xO$ films decreases from 3.285 eV to 3.271 eV. This phenomenon may be attributed to the change in the energy band structure in the ZnO film when Cu ions are incorporated into the ZnO lattice. An exchange interaction occurs between the valence band/conduction band electrons of ZnO and the local d-electrons of Cu ions replacing Zn ions. This exchange interaction introduces a new shallow energy level between the valence band and conduction band of ZnO, resulting in a reduction in the band gap of ZnO [28]. The transmittance decreases with increased Cu content, and the bandgap energy reduces as Cu content increases. The observed correlation between the bandgap and Cu content is likely influenced by the microstructure changes arising from the incorporation of Cu ions.

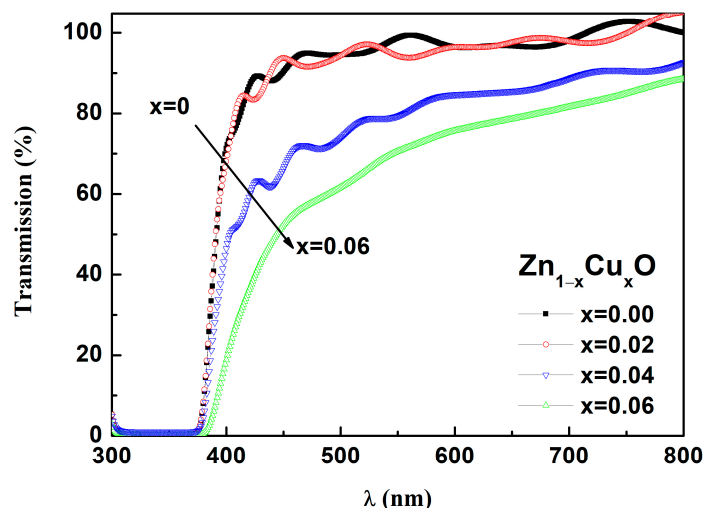


Figure 5. Spectra of optical transmittance for $Zn_{1-x}Cu_xO$.

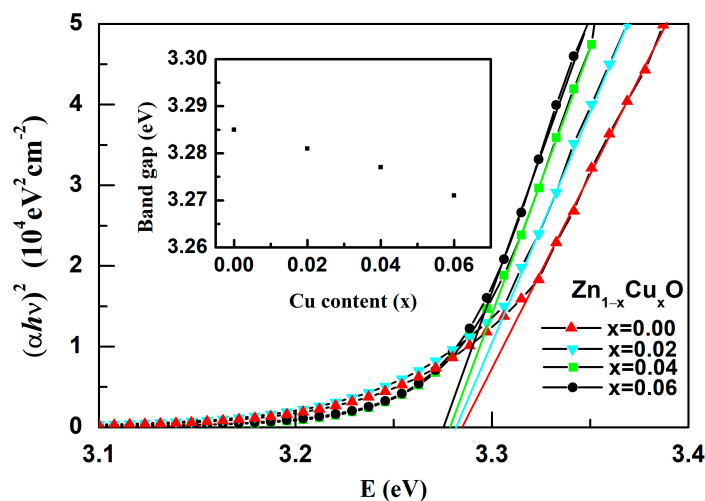


Figure 6. The curves of $(\alpha hv)^2$ vs. E_g for $Zn_{1-x}Cu_xO$. The inset is Cu doping amount vs. bandgap energy.

Figure 7 illustrates the bipolar I-V switching curves of $Zn_{1-x}Cu_xO$ films during the initial formation at 5 V in RRAM, with green arrows indicating the direction of the voltage sweep. The compliance current is controlled at 10 mA. RRAM devices can be operated using LRS-HRS switching cycles up to 100 times without losing the electric properties. The real image of $Zn_{1-x}Cu_xO$ films' RRAM device is shown in Figure 7a. The RRAM setup process involves shifting the device into the LRS with a high forward bias of the control voltage. The reset process is to reduce the operating current of the LRS and provide a negative bias voltage to the reset voltage to transition to the HRS state, showing a bipolar resistance change characteristic. According to the bipolar I-V switching curve of the $Zn_{1-x}Cu_xO$ film in Figure 7, the set voltages are 1.1V (0%), 1.2V (2%), 3V (4%), and 1.5V (6%), respectively. In addition, the reset voltages are $-0.9V$ (0%), $-1.4V$ (2%), $-2.8V$ (4%), and $-1.5V$ (6%), respectively. The LRS and HRS properties of RRAM can be explained by the formation and destruction of conductive filaments composed of oxygen vacancies [2–5]. The switching of RRAM can be explained by two resistance states (HRS and LRS), the basic mechanism of which is shown in Figure 8. The SET process is initiated when an external positive voltage is applied to the top electrode (Ag), as shown in Figure 8. During this process, oxygen anions (O^{2-}) migrate away from their original sites towards the top electrode, creating oxygen vacancies in their place. As these oxygen vacancies cluster together, they align and form conductive filaments between the top and bottom electrodes, switching the RRAM device from HRS to LRS. Conversely, the RESET process occurs when the polarity of the applied bias voltage is changed, leading to the breaking of conductive filaments in the HRS state. Some partially occupied oxygen vacancies below the top electrode are refilled with oxygen anions, converting them back into regular oxygen sites. Figure 7 provides a comparison of the switched resistance properties for $Zn_{1-x}Cu_xO$ thin films in RRAM devices at different Cu concentrations. The RRAM device with 6% exhibits the highest ratio of LRS/HRS and a higher value of resistance in a state of HRS. When an external positive voltage is applied to the top electrode, the oxygen vacancies gather and arrange to connect the top and bottom metal electrodes, and electrons can be transferred near the oxygen vacancies by hopping, thus forming a conductive filament. On the contrary, when the polarity of the applied bias voltage is changed, some partially occupied oxygen vacancies under the top electrode are refilled by oxygen anions, resulting in the destruction of the oxygen vacancies forming the conductive filament. At this time, the device will change from a high current state to a low current state. The higher the number of destroyed oxygen vacancies, the higher the LRS/HRS ratio will be. Therefore, the highest LRS/HRS ratio of the 6% RRAM device should be attributed to the formation of conductive filaments and the destruction of more oxygen vacancies in 6% Cu-doped ZnO. The higher the number of oxygen vacancies destroyed, the lower the low current state, and, thus, the higher the LRS/HRS ratio. In addition, the grain size of $Zn_{1-x}Cu_xO$ decreases with increasing Cu doping in the SEM analysis, which means there are more grain boundaries within the material. The grain boundaries typically exhibit higher electrical conductivity than the interior of grains in polycrystalline materials. The doping of copper can promote the formation of carrier transmission paths at the grain boundaries of $Zn_{1-x}Cu_xO$ and can also increase the carrier concentration within the $Zn_{1-x}Cu_xO$ material. This means that more carriers are available for transmission, which can lead to a lower resistive resistance state (LRS) and, thus, improve the LRS/HRS ratio and enhance the switching performance [29].

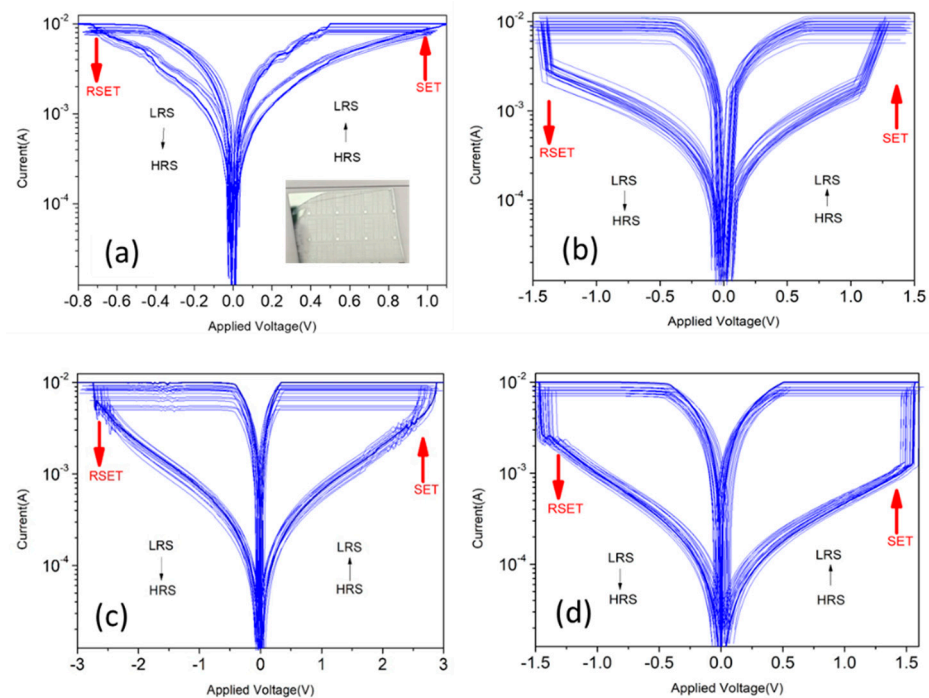


Figure 7. The switching curves of I–V of $\text{Zn}_{1-x}\text{Cu}_x\text{O}$ RRAM of (a) $x = 0$, (b) $x = 2\%$, (c) $x = 4\%$, and (d) $x = 6\%$ (inset shows the real device image in (a)).

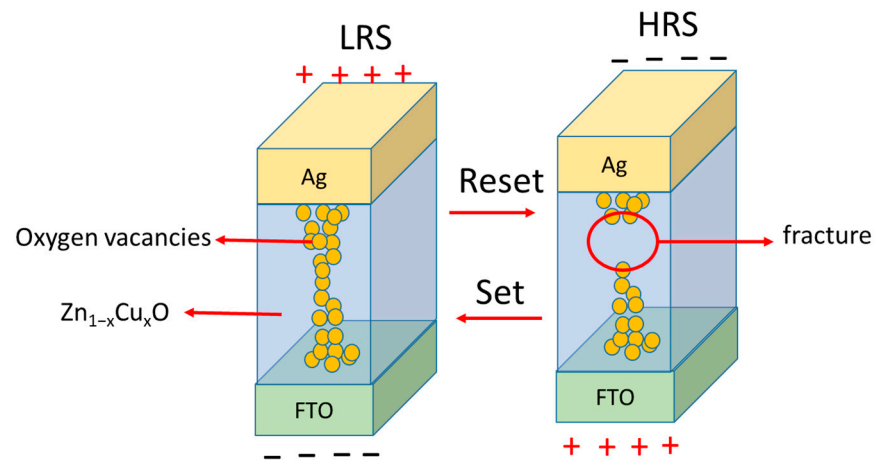


Figure 8. Schematic diagram of mechanisms of LRS and HRS for $\text{Ag}/\text{Zn}_{1-x}\text{Cu}_x\text{O}/\text{FTO}$ RRAM device.

Figure 9 displays the $\ln I$ versus $\ln V$ plot of the $\text{Zn}_{1-x}\text{Cu}_x\text{O}$ thin film, which is used to analyze the carrier conduction mechanism and understand the initial conductive filament formation process in the set/reset states of a metal–insulator–metal (MIM) structure. In the set state, the conduction path of the filaments is primarily influenced by the presence of oxygen vacancies in the Cu-doped ZnO films. The IV curves for the low resistance state (LRS) of all samples show slopes of approximately 0.98–0.99, indicating an ohmic conduction mechanism where the current is linearly dependent on the applied voltage. As the voltage increases, a stepwise increase in current is observed. On the other hand, in Figure 9b–d, the curves' slopes in the high electric field region of the high resistance state (HRS) are approximately 7.27–8.2, and the current rises sharply with the voltage. This suggests that the accumulation of oxygen vacancies in Cu-doped ZnO films enables carriers to be transported through traps located at different energy levels, leading to the

trap-assisted tunneling (TAT) mechanism responsible for this IV behavior [30–32]. Current density dominated by TAT can be expressed as:

$$J_{TAT} = AE^2 \exp\left[-\frac{B}{E}\right] \quad (1)$$

$$A = \frac{q^3 m}{16\pi^2 \hbar m^* \phi_t} \quad (2)$$

$$B = \frac{4\sqrt{2m^*}}{3\hbar q} \phi_t^{3/2} \quad (3)$$

where m^* is the effective mass of the electron, \hbar is Planck's constant, m is the mass of the electron in free space, and ϕ_t is the barrier height of the trap.

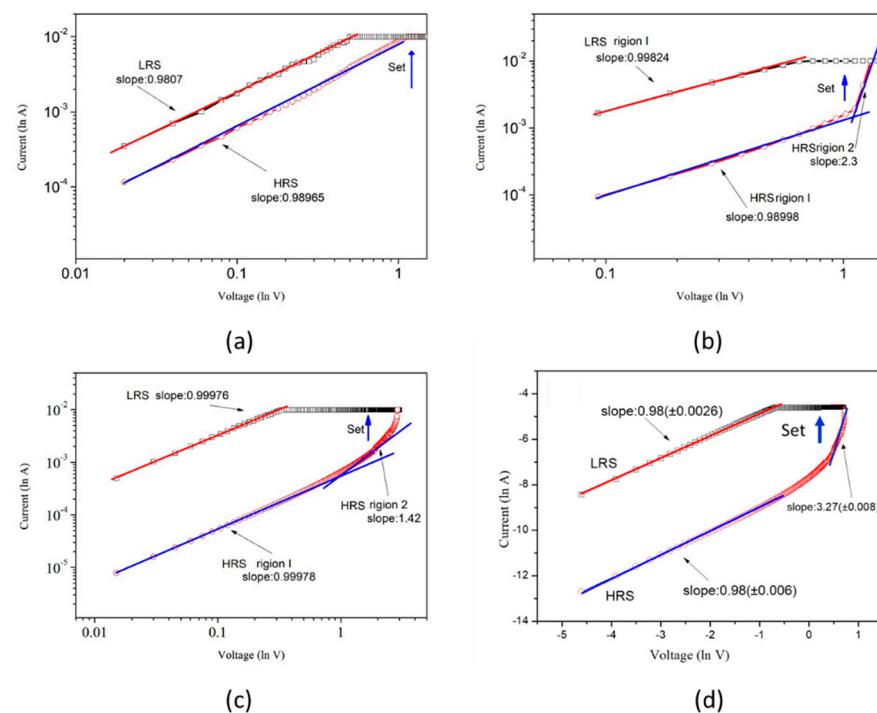


Figure 9. The curves of I – V for $Zn_{1-x}Cu_xO$ RRAM for the $\ln I$ – $\ln V$ curve of (a) $x = 0$, (b) $x = 2\%$, (c) $x = 4\%$, and (d) $x = 6\%$.

From the above results, the switching retention and endurance characteristics of the 6% Cu-doped ZnO thin film RRAM device are shown in Figure 10. It can be seen from the results that the 6% Cu-doped ZnO thin film RRAM device exhibits a stable state in more than one million switching cycles in Figure 10a. And the relationship between the resistance and switching time between the HRS and LRS states of the RRAM device can be clearly observed. RRAM devices also exhibit typical bipolar switching behavior and memory ratios greater than 10^3 HRS/LRS. In addition, the endurance characteristics of the 6% Cu-doped ZnO thin film RRAM device are shown in Figure 10b. There is no significant change in the on/off ratio switching behavior cycling versus time curves of the RRAM device over 10^3 s.

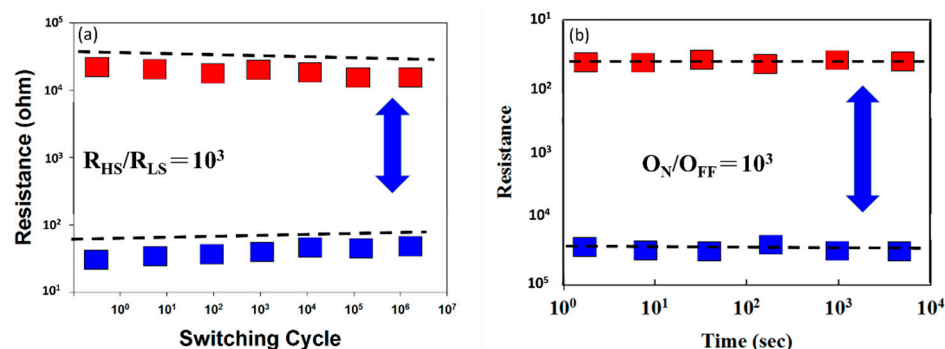


Figure 10. Switching endurance results of 6% Cu-doped ZnO film RRAM device showing (a) retention properties and (b) endurance properties.

4. Conclusions

Zn_{1-x}Cu_xO films were deposited on FTO substrates fabricated using the sol-gel process. The crystal structure, optical and resistive switching properties of Zn_{1-x}Cu_xO were studied and analyzed. The intensity of the (002) peaks of the Zn_{1-x}Cu_xO increased with an increase in doping of Cu from x=0 to x=0.06. Moreover, as the Cu content increased, the intensity of the ultraviolet emission and the yellow-green light emission peaks increased in the photoluminescence spectrum of Zn_{1-x}Cu_xO film. It was found that the Zn_{1-x}Cu_xO thin film RRAM exhibits the ohmic conduction mechanism and the trap-assisted tunneling (TAT) mechanism in the low electric field region (LRS) and high electric field region (HRS), respectively. RRAM devices based on 6% Cu-doped ZnO films exhibited the highest LRS/HRS ratio and higher HRS state resistance.

Author Contributions: M.-C.K. and J.-H.W. conceived and designed the experiments. M.-Z.L. prepared the materials. M.-C.K. and M.-Z.L. performed the experiments. M.-C.K. and K.-H.C. analyzed the data. M.-C.K. and J.-H.W. wrote the manuscript. All authors have read and agreed to the published version of the manuscript.

Funding: This work was supported by the National Science Council of the Republic of China under Contract No. NSC MOST 111-2637-E-164-002.

Data Availability Statement: Not applicable.

Conflicts of Interest: The founding sponsors had no role in the design of the study; in the collection, analyses, or interpretation of data; in the writing of the manuscript, and in the decision to publish the results.

References

- Li, Y.T.; Long, S.B.; Zhang, M.H.; Liu, Q.; Shao, L.B.; Zhang, S.; Wang, Y.; Zuo, Q.Y.; Liu, S.; Liu, M. Resistive switching properties of Au/ZrO₂/Ag structure for low-voltage nonvolatile memory applications. *IEEE Electron. Device Lett.* **2010**, *31*, 117–119.
- Guo, Y.; Robertson, J. Materials selection for oxide-based resistive random access memories. *Appl. Phys. Lett.* **2014**, *105*, 223516–223518. [[CrossRef](#)]
- Puglisi, F.M.; Larcher, L.; Bersuker, G.; Padovani, A.; Pavan, P. An empirical model for RRAM resistance in low- and high-resistance states. *IEEE Electron Device Lett.* **2013**, *34*, 387–389. [[CrossRef](#)]
- Zhuge, F.; Peng, S.; He, C.; Zhu, X.; Chen, X.; Liu, Y.; Li, R. Improvement of resistive switching in Cu/ZnO/Pt sandwiches by weakening the randomness of the formation/rupture of Cu filaments. *Nanotechnology* **2011**, *22*, 275204–275208. [[CrossRef](#)]
- Ke, J.J.; Wei, T.C.; Tsai, D.S.; Lin, C.H.; He, J.H. Surface effects of electrode-dependent switching behavior of resistive random-access memory. *Appl. Phys. Lett.* **2016**, *109*, 131603–131606. [[CrossRef](#)]
- Chang, W.-Y.; Lai, Y.-C.; Wu, S.-F.; Wang, F.; Chen, F.; Tsai, M.-J.; Tsai, M.-J. Unipolar resistive switching characteristics of ZnO thin films for nonvolatile memory applications. *Appl. Phys. Lett.* **2008**, *92*, 022110–022113. [[CrossRef](#)]
- Xu, N.; Liu, L.; Sun, X.; Liu, X.; Han, D.; Wang, Y.; Han, R.; Kang, J.; Yu, B. Characteristics and mechanism of conduction/set process in TiN/ZnO/Pt resistance switching random-access memories. *Appl. Phys. Lett.* **2008**, *92*, 92232112–92232113. [[CrossRef](#)]
- Kim, S.; Moon, H.; Gupt, D.; Yoo, S.; Choi, Y.K. Resistive Switching Characteristics of Sol-Gel Zinc Oxide Films for Flexible Memory Applications. *IEEE Electron. Device Lett.* **2009**, *56*, 696–699. [[CrossRef](#)]

9. Villafuerte, M.; Heluani, S.P.; Juarez, G.; Simonelli, G.; Braunstein, G.; Duhalde, S. Electric-pulse-induced reversible resistance in doped zinc oxide thin film. *Appl. Phys. Lett.* **2007**, *90*, 052105. [[CrossRef](#)]
10. Zhang, X.T.; Liu, Y.C.; Zhang, J.Y.; Lu, Y.M.; Shen, D.Z.; Fan, X.W.; Kong, X.G. Structure and photoluminescence of Mn-passivated nanocrystalline ZnO thin films. *J. Cryst. Growth* **2003**, *254*, 80–85. [[CrossRef](#)]
11. Xu, H.T.; Kim, D.H.; Zhao, X.H.; Ying, L.; Zhu, M.Y.; Lee, B.; Liu, C. Effect of Co doping on unipolar resistance switching in Pt/Co:ZnO/Pt structures. *J. Alloys Compd.* **2016**, *658*, 806–812. [[CrossRef](#)]
12. He, S.; Hao, A.; Qin, N.; Bao, D. Unipolar resistive switching properties of Pr-doped ZnO thin films. *Ceram. Int.* **2017**, *43*, S474–S480. [[CrossRef](#)]
13. Xu, D.; Xiong, Y.; Tang, M.; Zeng, B. Top electrode-dependent resistance switching behaviors of lanthanum-doped ZnO film memory devices. *Appl. Phys. A* **2014**, *114*, 1377–1381. [[CrossRef](#)]
14. Chiu, F.C.; Yang, M.Y. Trap characterization and conductance quantization in phosphorus-doped ZnO memory devices. *Vacuum* **2017**, *140*, 42–46. [[CrossRef](#)]
15. Zhu, X.J.; Su, W.J.; Liu, Y.W.; Hu, B.L.; Pan, L.; Lu, W.; Zhang, J.D.; Li, R.W. Observation of Conductance Quantization in Oxide-Based Resistive Switching Memory. *Adv. Mater.* **2012**, *24*, 3941–3946. [[CrossRef](#)]
16. Peng, H.Y.; Li, G.P.; Ye, J.Y.; Wei, Z.P.; Zhang, Z.; Wang, D.D.; Xing, G.Z.; Wu, T. Electrode dependence of resistive switching in Mn-doped ZnO: Filamentary versus interfacial mechanisms. *Appl. Phys. Lett.* **2010**, *96*, 192113–192115. [[CrossRef](#)]
17. Yang, Y.C.; Pan, F.; Liu, Q.; Liu, M.; Zeng, F. Fully Room-Temperature-Fabricated Nonvolatile Resistive Memory for Ultrafast and High-Density Memory Application. *Nano Lett.* **2009**, *9*, 1636–1643. [[CrossRef](#)]
18. Dietl, T.; Ohno, H.; Matsukura, F.; Cibert, J.; Ferrand, D. Zener model description of ferromagnetism in zinc-blende magnetic semiconductors. *Science* **2000**, *287*, 1019–1022. [[CrossRef](#)]
19. Wu, L.; Hou, T.J.; Wang, Y.; Zhao, Y.F.; Guo, Z.Y.; Li, Y.Y.; Lee, S.T. First-principles study of doping effect on the phase transition of zinc oxide with transition metal doped. *J. Alloys Compd.* **2012**, *541*, 250–255. [[CrossRef](#)]
20. Iribarren, A.; Hernandez-Rodriguez, E.; Maqueira, L. Structural, chemical and optical evaluation of Cu-doped ZnO nanoparticles synthesized by an aqueous solution method. *Mater. Res. Bull.* **2014**, *60*, 376–381. [[CrossRef](#)]
21. Mohan, R.; Krishnamoorthy, K.; Kim, S.J. Enhanced photocatalytic activity of Cu-doped ZnO nanorods. *Solid State Commun.* **2012**, *152*, 375–380. [[CrossRef](#)]
22. Srinivasan, N.; Revathi, M.; Pachamuthu, P. Surface and optical properties of undoped and Cu doped ZnO nanostructures. *Optik* **2017**, *130*, 422–426. [[CrossRef](#)]
23. Hull, A.W. A new method of X-ray crystal analysis. *Phys. Rev.* **1917**, *10*, 661–696. [[CrossRef](#)]
24. Patil, V.L.; Vanalakara, S.A.; Patil, P.S.; Kim, J.H. Fabrication of nanostructured ZnO thin films based NO₂ gas sensor via SILAR technique. *Sens. Actuators B Chem.* **2017**, *239*, 1185–1193. [[CrossRef](#)]
25. Singh, M.; Ambedkar, A.K.; Tyagi, S.; Kumar, V.; Yadav, P.; Kumar, A.; Gautam, Y.K.; Singh, B.P. Room temperature photoluminescence and spectroscopic ellipsometry of reactive co-sputtered Cu-doped ZnO thin films. *Optik* **2022**, *257*, 168860–168871. [[CrossRef](#)]
26. Mustafa, G.; Srivastava, S.; Aziz, M.K.; Kanaoujiya, R.; Rajkumar, C. Photosensitivity and structural properties of vanadium-doped ZnO and ZnO nanoparticle at various calcined temperature. *Mater. Today Proc.* **2023**, online ahead of print. [[CrossRef](#)]
27. Ma, L.; Ai, X.; Huang, X.; Ma, S. Effects of the substrate and oxygen partial pressure on the microstructure and optical properties of Ti-doped ZnO thin films. *Superlattices Microstruct.* **2011**, *50*, 703–712. [[CrossRef](#)]
28. Ghorbali, R.; Essalah, G.; Ghoudi, A.; Guermazi, H.; Guermazi, S.; El Hdiy, A.; Benhayoune, H.; Duponchel, B.; Oueslati, A.; Leroy, G. The effect of (In, Cu) doping and co-doping on physical properties and organic pollutant photodegradation efficiency of ZnO nanoparticles for wastewater remediation. *Ceram. Int.* **2023**, *49*, 33828–33841. [[CrossRef](#)]
29. Deuermeier, J.; Wardenga, H.F.; Morasch, J.; Siol, S.; Nandy, S.; Calmeiro, T.; Klein, A.; Fortunato, E. Highly conductive grain boundaries in copper oxide thin films. *J. Appl. Phys.* **2016**, *119*, 235303–235308. [[CrossRef](#)]
30. Hsu, C.C.; Chen, Y.T.; Chuang, P.Y.; Lin, Y.S. Abnormal volatile memory characteristic in normal nonvolatile ZnSnO resistive switching memory. *IEEE Trans. Electron. Devices* **2018**, *65*, 2812–2819. [[CrossRef](#)]
31. Chanana, R.K. Determination of electron and hole effective masses in thermal oxide utilizing an n-channel silicon MOSFET. *IOSR J. Appl. Phys.* **2014**, *6*, 1–7. [[CrossRef](#)]
32. Yu, S.; Guan, X.; Wong, H.-S.P. Conduction mechanism of TiN/HfO_x/Pt resistive switching memory: A trap-assisted-tunneling model. *Appl. Phys. Lett.* **2011**, *99*, 063507. [[CrossRef](#)]

Disclaimer/Publisher's Note: The statements, opinions and data contained in all publications are solely those of the individual author(s) and contributor(s) and not of MDPI and/or the editor(s). MDPI and/or the editor(s) disclaim responsibility for any injury to people or property resulting from any ideas, methods, instructions or products referred to in the content.